

# Identification of Multiscale Spatial Structure of Lunar Impact Crater: A Semivariogram Approach

Jiao Wang , Dongping Ming , and Weiming Cheng 

**Abstract**—Identifying the spatial structure of lunar impact craters is necessary to increase our understanding of past geologic processes on the Moon. However, detecting multiscale spatial structures of craters in images in appropriate resolutions using optimum scale parameters has not been quantified. This article presents a semivariogram approach for this purpose. The range of the semivariogram model represents the minimum average size of the crater type detected in an image of a spatial resolution. The feature lag distances of the semivariogram model indicate that a series of appropriate spatial resolutions rather than a single spatial resolution are required to address multiscale lunar impact crater structures. The optimum scale parameters for delineating multiscale crater structures in segmentation are constrained by the range and feature lag distances derived from semivariogram of the corresponding image in a certain spatial resolution. This article fills the gap in quantifying multiscale spatial structure of impact craters using semivariogram analysis for optimizing object-based crater mapping.

**Index Terms**—Lunar impact crater, multiscale spatial structure, optimum resolution, scale parameter, semivariogram.

## I. INTRODUCTION

MAPPING geologic features is one of the most impressive methods to investigate the lunar surface directly, in which the spectral reflectance of geologic features on remote sensing images is well recorded [1], [2]. Among the most studied geologic features in the solar system, different types of craters yield important information about past and present geologic processes and provide information about the relative ages of observed geologic formations [3]. The transition of crater types provides significant insights into the changes in lunar surfaces

occurring with time and clues about attendant impacting and geologic processes [4]. From a systematic perspective, different crater types can be arranged in the form of a spatial hierarchical structure [5], [6], in which a certain crater appears at a specific spatial scale with subsequent scale levels of crater types beneath it. The process of the morphological changes observed in a hierarchical structure of lunar impact craters is a function of variability in the scale [7]. In remote sensing, the spatial resolution is the primary measurement of scale [8]. The separation of the intrinsic hierarchical structure of craters into discrete levels of crater types and morphologically representative objects can be achieved by performing multiscale lunar surface segmentations [9]. Although existing works have used hand-crafted filters relying on domain knowledge or training examples to map craters artificially or automatically, they have not taken information on spatial structures in the process of mapping. The selection of optimum spatial resolutions and scale parameters for segmentation is necessary and significant to quantify the evolutionary information behind a crater's spatial structure.

Remote sensing scientists mapped various types of objects on planetary surfaces to collect information about their status [10], composition, distribution, dynamics [11], [12] and species [13], and related applications [14]–[16] on the basis of selecting appropriate spatial resolutions and scale parameters for image processing [17]. An appropriate image spatial resolution is the optimum pixel size to capture the homogeneity of object properties in a single pixel. Previous works adequately documented that the spatial variation observed in objects is a function of the variability in scale such that a single spatial scale cannot provide a complete view of the actual spatial structures [18]–[20]. One potential solution is arbitrarily choosing one spatial scale for simplicity [21]–[23]. For example, most mangrove studies using remote sensing techniques produce single scale-specific information, depending on the spatial resolution of the datasets used [24]. For spatial structures characterizing and comparing by aggregated data, selecting multiple optimum spatial resolutions becomes a challenge. The scale parameter in image segmentation, in relation to image spatial resolution, is the maximum allowable degree of heterogeneity within an object by changing the size of the object [25]. The quality of segmentation depends on image spatial resolution and user-defined parameter settings, both of which should be scaled to capture the spatial variation observed within the object [26]. However, one of the main issues in parameter selection is ensuring that the image object types are consistently mapped at one scale but hierarchically fit with types that apply to other scales.

Manuscript received August 4, 2020; revised November 24, 2020 and January 15, 2021; accepted February 1, 2021. Date of publication February 9, 2021; date of current version March 9, 2021. This work was supported in part by the National Natural Science Foundation of China under Grant 41801361, in part by the Fundamental Research Funds for the Central Universities under Grant 2652019027, in part by a Grant from the State Key Laboratory of Resources and Environmental Information System, in part by the B-type Strategic Priority Program of the Chinese Academy of Sciences under Grant XDB41000000, and in part by the China Postdoctoral Science Foundation under Grant 2018M631535. (Corresponding author: Jiao Wang.)

Jiao Wang is with the School of Information Engineering, China University of Geosciences, Beijing 100083, China, and also with the State Key Laboratory of Resources and Environmental Information System, Institute of Geographic Sciences and Natural Resources Research, Chinese Academy of Sciences, Beijing 100101, China (e-mail: jiaowang@cugb.edu.cn).

Dongping Ming is with the School of Information Engineering, China University of Geosciences, Beijing 100083, China (e-mail: mingdp@cugb.edu.cn).

Weiming Cheng is with the State Key Laboratory of Resources and Environmental Information System, Institute of Geographic Sciences and Natural Resources Research, Chinese Academy of Sciences, Beijing 100101, China (e-mail: chengwm@lreis.ac.cn).

Digital Object Identifier 10.1109/JSTARS.2021.3058255

To solve the issue of selecting optimum spatial resolutions and scale parameters, various statistical measures have been applied, including local variance [27], [28], the variograms [29], [30], and wavelet transform [31], [32]. Among these methods, a semivariogram, a commonly used analysis tool in geostatistics, can be used to translate significant scales in spatial variation into image spatial resolutions [33]. Semivariograms have been widely used in terrestrial object mapping in various scenarios from image data, for example, in forest structure [34]–[37], soil properties [38]–[40], and landscape structure [30], [41]–[43]. Researchers mainly focus on calculating the semivariances between image cells to segment objects and classify object types [44], [45]. However, these have not been used to quantify the spatial hierarchical structure of lunar impact craters by determining appropriate image spatial resolutions and segment scale parameters.

This article aims to examine the spatial structure of lunar impact craters on remote sensing imagery to determine multispatial resolutions and scale parameters for crater mapping studies. A proper understanding of the spatial dependence of crater structures is essential to avoid the potential errors arising from heterogeneity and homogeneity in upscaling or downscaling mapping processes. We adopt the geostatistical method of semivariogram analysis on multiresolution imageries for the following purposes.

- 1) Identify the spatial structure of lunar impact crater forming a hierarchical system.
- 2) Determine the optimum resolutions of specific crater types in the multiscale spatial structure.
- 3) Validate optimum scale parameters for detecting certain crater types in the crater structure.

## II. DATA AND METHOD

### A. Data and Study Area

The image data used for examining crater spatial structures were obtained from the Chang'E-2 CCD stereoscopic camera at an altitude of 100 km in orbit. A 7-m resolution full-Moon digital orthophoto map was produced by the Chang'E-2 images [46]. Also, a set of very high spatial resolution (0.5–2 m/pixel) images from the narrow angle camera (NAC) of the lunar reconnaissance orbiter camera (LROC) was also used to measure the dimension of craters in detail [47]. NAC images in 1-m pixel size were resampled to multiple specific-scale images under different illumination conditions and moderate spatial resolution (120, 50, 20, and 7 m/pixel). We selected this series of resampled pixel sizes because they were approximate to the currently available image datasets from Chang'E-1, Chang'E-2, SELENE-1, and LRO Lunar exploration programs to detect specific details of crater types [48], [49]. The image datasets were preprocessed in MATLAB R2014a and ENVI 5.1 image processing software.

This research was performed in the selected area of Ptolemaeus LM 77, named in the Lunar Map Series between 10°W–10°E and 0°–15°S [50]. The study area is selected because: it consists of two major geomorphological units of the moon: mare plain and cratered highland; it contains craters with a wide range of geomorphological characteristics; and it is covered by

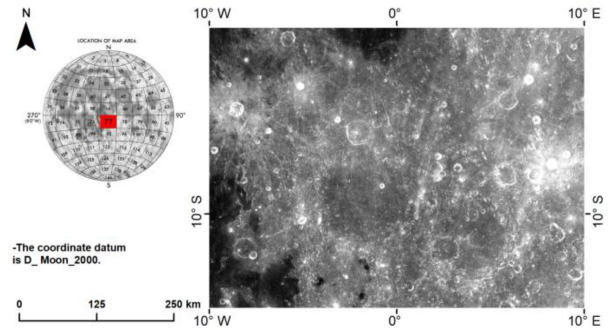


Fig. 1. Study area Ptolemaeus LM 77 on a 7-m resolution Chang'E-2 panchromatic image. The global location is marked by the red rectangle.

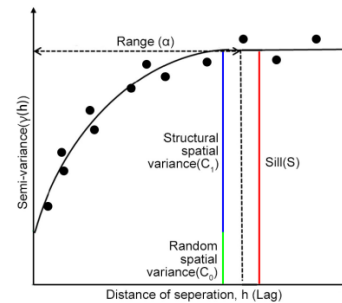


Fig. 2. Schematic diagram of the semivariogram with three key parameters: The green nugget variance ( $c_0$ ), the red sill ( $c_0 + c_1$ ), and the dashed range ( $\alpha$ ) of spatial autocorrelation.

multiresolution imageries. All of the above guarantee a robust method execution (see Fig. 1).

### B. Method

The semivariogram method is widely used for characterizing the spatial variability of regionalized variables [51]. A semivariogram  $\gamma(h)$  is defined as half of the average squared difference of values between points separated at distance ( $h$ ), which is calculated as half a variogram [52]. For the applications of remote sensing, the semivariogram examines the relationship between the digital number (DN) or pixel value of  $n$  pixel pairs across varying lag distances  $h$  [53]. The typical semivariance  $\gamma(h)$  is

$$\gamma(h) = \frac{1}{2n} \sum \{DN(x) - DN(x+h)\}^2 \quad (1)$$

where  $\gamma(h)$  is half of the mathematical expectation of the squared differences of pixel pair values at a lag distance ( $h$ ), and DN refers to pixel values in the image. Thus,  $\gamma(h)$  estimates the variability of DNs as a function of spatial separation [54], [55].

As shown in Fig. 2, each distance ( $h$ ) is paired with a  $\gamma(h)$  value, and a set of  $\gamma(h)$  scattered values can be obtained by transforming ( $h$ ). Fitting a continuous mathematical model to the discrete values to derive the appropriate sill, range and nugget from the discrete experimental data is necessary to quantify spatial patterns of objects. For this article, we applied a spherical model commonly used for natural system studies [56], [57]. In the remote sensing image, the larger  $\gamma(h)$  is, the less the spectral similarities of pixels are. The semivariogram exhibits three

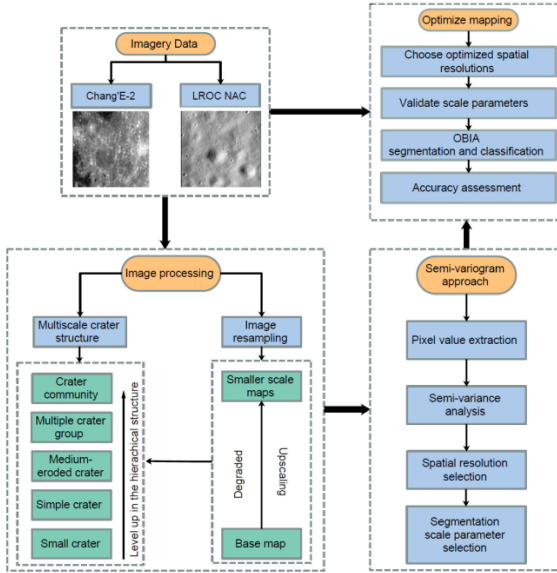


Fig. 3. Flowchart of the developed method consists of three parts: Image processing, semivariogram analysis, and mapping optimization.

important parameters that reflect the characteristics of spatial variance: nugget variance ( $c_0$ ), sill ( $c_0 + c_1$ ), and range ( $\alpha$ ). The range is the distance where the variogram reaches the sill and represents the maximum spatial distance at which the dataset can still demonstrate spatial homogeneity [32]. The most important factor for this study was the range of the semivariogram, which would indicate the size of objects on the lunar surface by grouping spatially autocorrelated pixels together following the sampling theorem [58]. Therefore, spatial resolution related to the range of the semivariogram could be defined. Then the scale parameters during image segmentation will adjust the size of image objects on the basis of appropriate spatial resolutions [45].

Fig. 3 shows the overall workflow of the developed method. The workflow consists of three parts. Image processing aims to create multiple-resolution images as a basis for extracting a hierarchical structure of lunar impact craters. To produce larger pixels, we reduced the resolution of the original 1-m image and averaged all of the original small pixels to make up the new big pixels. The spatial structure of lunar impact craters was detected on images at different pixel sizes on the basis of significant spatial variation in spectral reflectivity. Then, the semivariogram models quantified the spatial structure of craters by determining the optimum pixel sizes and estimating segmentation parameters for crater types. Next, pixel values were extracted in ArcGIS Desktop 10.5, and the semivariance calculation was executed in MATLAB R2014a. In this article, variograms and fitted models are used to characterize the spatial variation in imageries representing different crater types, which help choose an appropriate combination of spatial resolutions for crater structure detection. Then, optimized mapping applies appropriate spatial resolutions and scale parameters to image datasets to validate the results of the semivariogram analysis under the framework of object-based image analysis (OBIA). Next, we adopt the method that integrates image resolution and scale parameters under the framework of OBIA in a 64-bit

version of eCognition Developer 8 to determine the segmented boundary of spatial structure of the lunar impact craters [59]. In the stage of segmentation, the stage, scale parameters derived from semivariogram analysis were selected to segment objects. The shape and color parameters within the segmentation algorithm were held constant at 0.1 and 0.9, respectively, to test the effect of the scale parameters from the semivariogram analysis on segmentation. The smoothness and compactness parameters were held constant at 0.5.

Finally, we assess the accuracy of the detected crater structure in five selected regions. The five evaluated factors are integrated by Chen *et al.* [60]–[62]: TDR, FDR, MDR,  $R_{in}$ , and  $R_{out}$ . SUM is the total number of impact craters in the region determined by the LU106016 catalog [63]. TD is the number of true detected craters, MD is the number of missing detected craters, and FD is the number of false detected craters. TDR and MDR are the rates of the number of true detected craters and missing detected craters to the total number of impact craters respectively. FDR is the rate of the number of false detected craters to the sum number of false detected craters and true detected craters [61]. TDR, FDR, and MDR are factors evaluating the results from the perspective of the numbers of detected craters.  $R_{in}$  is the area percentage of the portion of the automatically extracted results in the manually extracted craters to the area of the manually extracted craters, whereas  $R_{out}$  is the area percentage of the portion of the automatically extracted results outside the manually extracted craters to the area of the manually extracted craters.  $R_{in}$  and  $R_{out}$  are factors evaluating the results from the perspective of the geometry of the detected craters.  $R_{in}$  approaching 1 and  $R_{out}$  approaching 0 suggest accurate detection [60], [62].

### III. RESULTS AND DISCUSSION

#### A. Crater Structure and Semivariogram Model

A significant spatial variation in spectral reflectivity was observed for the lunar impact craters on images at different pixel sizes between 1- and 120 m. In the study area, the spatial structures of lunar impact craters were detected on the basis of different spatial resolutions and consisted of five levels of crater types including: small crater, simple crater, medium-eroded crater, multiple crater group, and crater community (see Fig. 4). Small craters comprised depression-like shapes pressed by fingers on soft sand. They are mostly scattered in the wall, bottom, and rim of the other craters and are especially distributed in the Mare. Simple craters comprised bowl-shaped depressions, where no clear boundary exists between the wall and bottom of the crater. They possess an uplifted rim and lack a central peak and terraced crater rim when they are fresh. As the diameter increased further, medium-eroded craters formed. Such craters include transitional craters and complex craters. Transitional craters lacked a central peak, but they possessed a shallower profile, eroded crater rim, or some terraced crater wall compared with simple craters. Complex craters generally exhibited a structurally complicated rim, a downfaulted annular trough, and an uplifted central area. The mentioned three crater types became complicated in morphological change but were not in a special positional relationship. Multiple-crater groups emphasized the positional relationship between the aforementioned crater types.

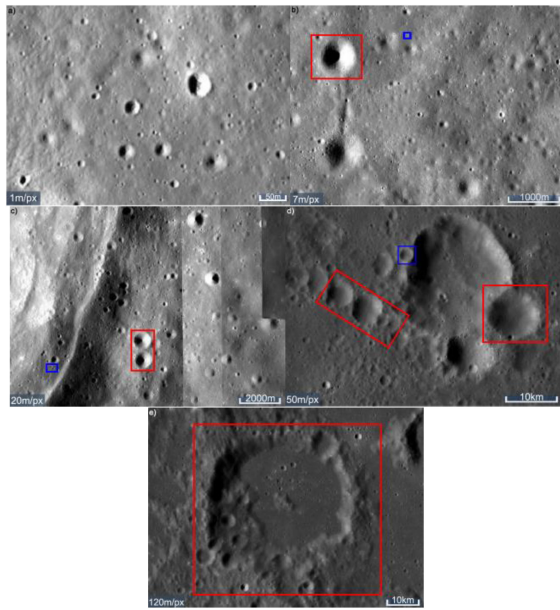


Fig. 4. Multiscale spatial structures of lunar impact craters. From the LM77 imagery, subimages in a series of pixel sizes were extracted. (a) Small craters in different sizes in the 1-m/pixel image. (b) Simple craters (an example in the red rectangle) and small craters (an example in the blue rectangle) in different sizes in the 7-m/pixel image. (c) Crater groups consist of small craters (an example in the red rectangle) and simple craters (an example in the blue rectangle). (d) Medium-eroded craters (an example in the blue rectangle) and crater groups (examples in red rectangles). (e) Crater community (an example in the red rectangle).

Here, the positional relationship included four types, that is, disjoint, tangent, intersected and contained, where the latter two were strictly in superposition. For disjoint crater groups, the gaps between craters were generally less than or almost equal to the diameter of the smallest crater in the group. Otherwise, they were just independent craters assigned to the above three types. The tangent and intersected crater groups were typically multiple-crater groups to stress the scale effect of detecting crater groups. Contained crater groups referred to medium-eroded craters containing small or simple craters inside of them. The highest level in the hierarchical structure of craters was the crater community. The difference between the crater community and the contained crater group was the size of the host crater and the number and size of the superimposed craters. For small and simple craters, the crater community could be crater chains or high-density crater groups. For medium-eroded craters, the host craters of the crater community were generally multi-ring or ghost craters with heavily eroded crater rims. The superimposed craters in the community ranged from small to complex craters in larger numbers than in the crater group. From small craters to crater communities, crater sizes increased, crater shapes became complex, the positional relationship between craters became complicated, and the spectral reflectivity of craters varied. The higher the spatial resolution, the smaller the identifiable crater. The hierarchical structure of craters demonstrated a clear multiscale context of the crater types and their relationships, which actuate a logical sequential mapping process.

The semivariogram models of the images at five different pixel sizes are shown in Fig. 5. The spatial structures of craters can be detected at a series of images with increasing pixel sizes.

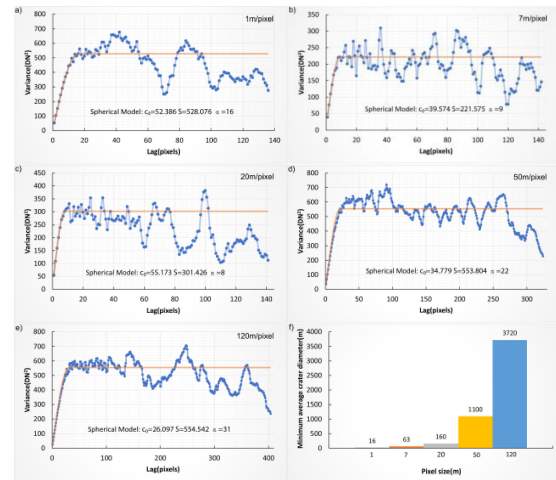


Fig. 5. (a)–(e) Semivariogram models of images at five different pixel sizes. Blue dots represent discrete experimental data, and the spherical model fits are presented as an orange solid line. The parameters of the spherical model are also shown in the graphs. (f) Average minimum crater size could be identified in different resolution images by analyzing the ranges of the semivariogram models. The label on the top of each bar is the average diameter of the smallest detected crater.

Next, the semivariogram models showed that the coarse images contained large objects (large variogram range), whereas the fine images contained predominantly small objects (small variogram range). Small craters approximately 16 m in diameter could be recognized using the 1-m image, whereas the minimum average crater diameter identified in the 120-m image is about 4 km. The minimum average crater diameters are about 70 m, 160 m, and 1 km, respectively, at image pixel sizes of 7, 20, and 50 m, respectively [see Fig. 5(f)]. The size of craters of the same type is not a specific value but floats in scope, and the range ( $\alpha$ ) of semivariograms from different resolution images represents the minimum average crater size for a certain crater type. The sills of the semivariogram models increasingly fluctuate except for the 1-m/pixel semivariogram model, which may be because a small pixel size contains more background information, leading to large semivariances. The semivariances in every semivariogram model showed periodic fluctuations, indicating the same crater type in various spatial relationships.

Variations within one crater type could occur at different spatial resolutions because topographical and morphological factors operate at different spatial scales [9]. Spatial differences in depth, slope aspect, and slope angle affect the distribution and pattern of certain crater types, specifically slope angle and depth, which exhibit distinct changes on the edge of a specific crater type. Morphological differences in crater shape and symmetry affect the spectral reflectivity of certain crater types in panchromatic images. Therefore, different geographical factors that caused the spatial variation on the lunar surface should be represented at different resolutions in a remote sensing image.

Impact craters are a very special types of geomorphological features. These can be abstracted as irregularly distributed circles with different diameters in space. The detection of its spatial structure can be summarized as the detection of the spatial pattern of 2-D random circles in images using the semivariogram method. In detecting the spatial pattern of 2-D random circles

in images, the mean, variance, calculating window size of the variance, and irregularity of the spatial distribution will affect the detection of the spatial pattern of features. In this study, the calculating window size of semivariance has remained consistent, whereas the wide diameter range and irregular spatial distribution of craters make relying only on the range ( $\alpha$ ) to identify the entire structure of an impact crater impossible. Periodic spatial patterns composed of the impact crater and its surface background are presented as periodic fluctuations on the semivariogram model curve. Therefore, in addition to the range ( $\alpha$ ), different levels of crater types in the spatial structures of crater can be obtained from the peaks of the curve periods. This is the basic principle of how a semivariogram model determines the spatial structure of an impact crater.

### B. Selecting Spatial Resolutions

The spatial structure of a crater contains heterogeneous spatial variations in different levels of crater types represented by spatially varied variograms. For small and simple craters, using the variogram against spatial resolutions to select an appropriate spatial resolution for analysis is reasonable. A mapper could use the semivariogram plot to determine that the spatial resolutions of 1, 7, and 20 m should be sufficient to adequately resolve the variation of interest. The middle level of the spatial structure contains medium-eroded craters and multiple-crater groups. Craters in this level are distributed in a wide diameter range. Hence, the semivariogram models of all pixel sizes exhibited fluctuations, suggesting that the spatial variation appeared in a range of scales for the same crater type. The suitable spatial resolutions for these two crater types reasonably represent their minimum average size. A high level crater community contains a maximum range of scales of spatial variation compared with other levels of crater types in the hierarchical spatial structure. In this situation, the mapper must accept that if the crater community as a whole is of interest, defining a single appropriate spatial resolution only represents the largest crater in the community. This is the most common problem because most remotely sensed scenes often contain a mixture of objects.

The range and sill height of a semivariogram illustrate the minimum average size of an identified crater and a specific class of pixel value variance in the image, respectively. Periodic peaks and troughs appear when the lag distance over the range implies a new positional relationship between main crater types and can be detected using appropriate pixel size images. Generally, the peak in a period corresponds to the size of a crater type, and the trough in a period corresponds to the size of the background of the same crater type. The peak at the 42 lag distance in the 1-m/pixel variogram model suggests a simple crater, whereas the peak at 60 indicates a crater group. The fluctuations in the semivariogram models of 7- and 20-m pixel sizes over the range ( $\alpha$ ) suggest that multiple-crater groups with craters approximately 500 m and 2 km in diameter can be identified. The size of medium-eroded craters is in a wide range ( $\geq 5$  km in diameter), so that 50- and 120-m/pixel images can be used for recognizing this level of crater structure. Craters approximately 10 km in diameter with eroded rims or multiple-crater groups can be detected at a lag distance of 180 in the 50-m/pixel

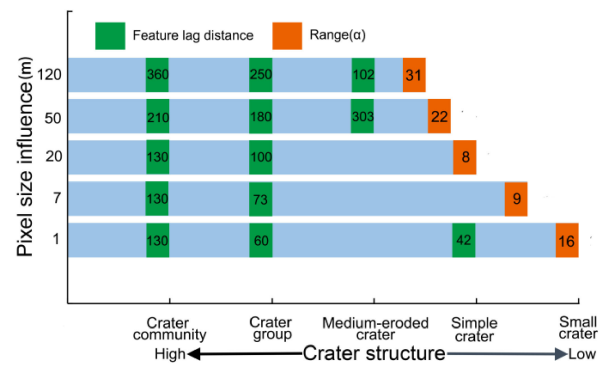


Fig. 6. Relationship among crater types, variogram ranges, and optimum pixel sizes to map crater structures. The orange bar represents the variogram range to map the average minimum crater on each resolution image. The green bar represents the feature lag distance to identify other crater types in the spatial structure.

image. Craters approximately 30 km in diameter with peak and terraced crater walls can be identified at a lag distance of 250, whereas multiring crater communities occur around the lag distance of 360 in the 120-m/pixel image. Fig. 6 shows that the medium-eroded impact crater can be identified from images with resolutions greater than 50 m, whereas craters less than 1 km in diameter cannot be extracted from images with resolutions greater than 50 m because they are too small to be recognized and their boundaries cannot be precisely located on images with big pixel sizes. Crater communities and groups are distributed in a relatively large-scale span, and their feature lag distances of the semivariogram grow with increasing resolution. So, optimum images with different resolutions should be selected according to the size of the crater community or group. Different ranges and feature lag distances correspond to different crater types and eventually form the spatial structure of lunar impact craters. The feature lag distances from high-resolution images can assist those from low-resolution images in differentiating specific levels of crater types (see Fig. 6).

Clearly, the use of a semivariogram selecting a single suitable spatial resolution for the whole spatial structure is misleading. This is also true if the objective is to select a single spatial resolution for the whole image of a study area from which subimages were taken. The main finding is that multiple-scale spatial variations in remotely sensed images make defining a spatial resolution for the spatial structure of craters problematic, when the region of interest contains multiple crater types rather than a specific crater. The semivariogram models presented in this article demonstrate that choosing a spatial resolution for a mixed crater type in remotely sensed images may be a complex task. Selecting a single appropriate spatial resolution may be difficult, and selecting a series of appropriate spatial resolutions to illustrate the spatial structures of a crater is instead wise. The range of the semivariogram can determine the minimum average size of different types of impact craters that can be extracted from remote sensing images of different resolutions, which provides criteria for selecting image data to be used for extracting and mapping impact craters. The periodic peaks of the semivariogram can determine the spatial patterns of the impact crater spatial structure in images with different resolutions,

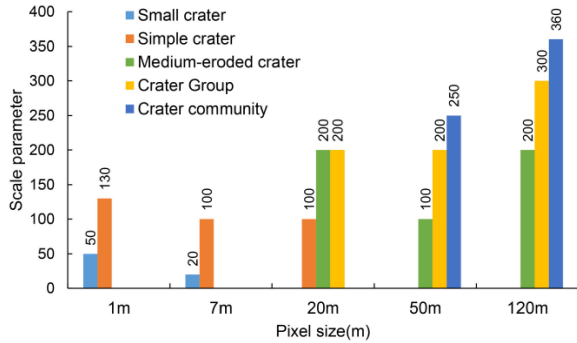


Fig. 7. Optimum scale parameters for crater segmentation in images with related resolutions.

which provide a database for identifying the scale parameters of the impact crater in image segmentation. In summary, we can choose the optimum image resolution for identifying different types of impact craters, and a series of optimum multiresolution images for constructing the spatial structure of impact craters.

### C. Selecting Scale Parameters

Image segmentation can separate craters of interest from other parts in the image to show the spatial structure of craters more explicitly. The scale parameter is the most important parameter in segmentation. Optimizing of the scale parameter relates to the selected pixel size of the image. The results of the segmentation of images at different scale parameters while holding other parameters constant under the frame of OBIA are presented in Fig. 7. Color vertical bars with various lengths indicate optimum scale parameters for different levels of crater types for the selected images of various pixel sizes. Small craters are suggested to be detected in 1- and 7-m/pixel high-resolution images with the scale parameters of 50 and 20, respectively, whereas crater communities are recognized in 50- and 120-m/pixel low resolution with the scale parameters of 250 and 360, respectively. The appropriate scale parameters for segmenting small craters become small with the increase of in image pixel size. Simple craters can be extracted from 1-, 7-, and 20-m/pixel images with the scale parameters of 130, 100, and 100, respectively. The optimum scale parameters for segmenting in 7- and 20-m/pixel images are the same. The optimum scale parameters for segmenting crater groups and communities are around  $200 \pm 100$ . A slight rise in the value of the scale parameters for crater community segmentation is due to the growing size of crater types occupying more pixels in low-resolution images. The scale parameters for medium-eroded craters and crater groups in 20-m/pixel images are the same. This may be because the craters in these two levels exhibit similar size ranges.

The feature lag distances of the semivariogram guide the selection of the optimum scale parameters. In Section III-B, the range ( $\alpha$ ) specifies the type of crater that can be optimally extracted from each resolution image, and it indicates the minimum average size of the corresponding crater type. Under this premise, the range ( $\alpha$ ) constrains the selection of the scale parameter as the bottom line. The determination of

TABLE I  
ACCURACY ASSESSMENT OF DETECTED CRATER STRUCTURE

Crater type	Resolution	Scale parameter	SUM	TD	MD	FD	TDR	MDR	FDR	$R_m$	$R_{out}$
Small	1m	50	55	50	5	9	90.9%	9.1%	15.3%	91.7%	1.2%
	7m	100	87	73	14	16	83.9%	16.1%	18.0%	96.6%	1.0%
Eroded	20m	200	22	16	6	5	72.7%	27.3%	23.8%	80.7%	13.6%
	50m	200	18	14	4	3	77.8%	22.2%	17.6%	82.1%	6.7%
Community	120m	360	4	3	1	0	75.0%	25.0%	0.0%	74.8%	19.4%

the scale parameter of a crater is performed by ensuring the optimal segmentation of the average level of the same type of crater, which is usually larger than the value of the range( $\alpha$ ). Under this condition, the principle of optimal segmentation ensures maximum homogeneity within the crater and maximum difference between craters. For example, the scale parameter 50 ensures that the small craters in the 1-m/pixel image are not oversegmented or undersegmented. In the 120-m/pixel image, the scale parameter 360 ensures that the boundary of the crater community is detected rather than recognizing those of low-level crater types because of oversegmentation. The scale parameters given here are for the optimal segmentation of the spatial structures of craters in the selected study area. The scale parameters will be distributed to other scopes if the study area and the crater types change. However, the results of the semivariogram analysis will determine the scale parameters in various situations.

The results derived from optimum resolutions and scale parameters in segmentation are tested by five factors integrated by Chen *et al.* [60]–[62]. Craters with different levels of spatial structures related to different image resolutions in five selected regions in Fig. 4 were separately evaluated. According to Table I, small craters in high-resolution images can be well detected and exhibit the highest TDR, whereas medium-eroded craters in the 20-m/pixel image are comparatively poorly detected and exhibit the lowest TDR. The evaluated results suggest that small craters are better recognized using high-resolution images with optimum scale parameters. For medium-eroded craters ranging in a wide size scope, smaller eroded craters are easily missed, and larger eroded craters are inclined to false detections. Although simple craters do not exhibit a high count accuracy, their geometric detection accuracy is the highest because their intact shape can be recognized from a proper image with optimum scale parameters. In contrast, the geometric detection accuracy of crater communities is the lowest. The heavily eroded rims and overlaid border craters of crater communities make the boundary confirmation difficult rather than counting challenging. The selected region only exhibits four sets of crater communities, which may be the reason for the low TDR.

This article focused on studying the coupling relationship among the spatial structures of craters, resolution of remote sensing optical images, and scale parameters. Some previous studies proposed various crater detection algorithms (CDAs) based on optical remote sensing images to detect the rims of impact craters, but they did not consider the spatial structure of craters. Convolutional neural network for crater detection (CraterCNN) [64] with high computational costs outperformed some existing methods and achieved up to 90% of the standard crater benchmark dataset by Bandeira *et al.* [65]. Then, the inception of the GoogLeNet architecture further improved the CraterCNN benchmark and achieve up to a 93% F1-Score [66]. Our method

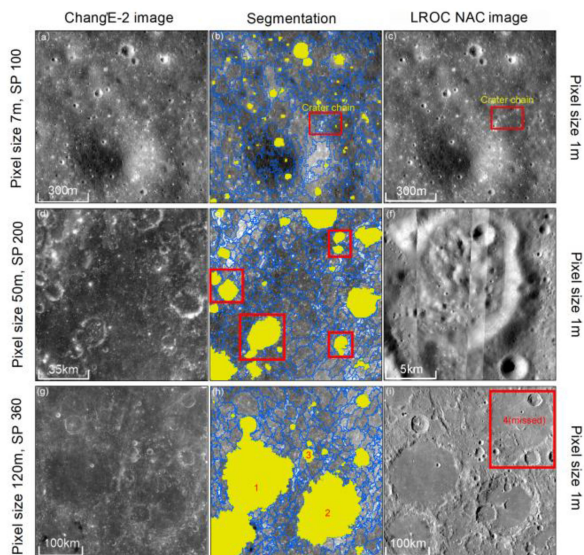


Fig. 8. Crater structure is segmented (blue polygons) and classified (yellow polygons). (a), (d), and (g) Images with different pixel sizes. (b) Simple craters are detected using the scale parameter of 100; the red rectangle in (b) and (c) mark out the rim of the whole crater chain but the inner rims of each simple crater in the chain are missing. (e) Four sets of crater groups are marked out. (f) Examples of missed small and simple craters lie in crater groups. (h) Three crater communities are obvious, but one ghost crater community in the upper right rectangle is missed in Fig. 8(i). (b), (e), (f) have the same scales as the original images (a), (d), (g).

for small crater detection was as good as these methods. Other studies presented CDAs on the basis of terrain analysis using relatively low-resolution images. Automated crater detection on Mars using deep learning methods achieved an approximately 25% false-positive rate and 25% false-negative rate [67]. The accuracy of the CDA proposed to detect different morphological craters on the basis of terrain analysis on the Moon was between 86.2% and 86.9% in three study areas.  $R_{in}$  and  $R_{out}$  were 84.4% and 8.9%, respectively [60], which were near to the average values of the same factors (85.2% and 8.4%, respectively) used in our method. In future studies, we may transmit our method integrating machine learning techniques on the basis of different data sources to clarify the relationship among the extraction of geomorphological features on extraterrestrial bodies, image quality, and segment thresholds.

The classification results derived from the optimum scale parameters in segmentation are shown in Fig. 8, in which selected examples with pixel sizes of 7, 50, and 120 m depict information on simple craters, crater groups and crater communities, respectively. An LROC NAC 1-m/pixel image is used as the ground truth to evaluate the quality of segmentation. High resolution images are usually used as the ground truth data for planet research, especially for those planets not inhabited by humans, where we lack enough and continued field data and aerial photographs. Simple craters are effectively extracted from the 7-m/pixel image using the optimum scale parameter [see Fig. 8(b)]. Simple craters standing out from the background or laid on the bottom or wall of bigger craters are all discriminated, even the ones overlapping with each other but with clear crater rims. For the small craters impacted as crater chains, this scale parameter only depicts the rim of the whole chain and misses

the inner rims in the chain [see Fig. 8(c)]. Four sets of double-crater groups are present in the 50-m pixel image marked by red rectangles. These represented four groups are in different sizes and shapes, which are well detected using the suggested scale parameter [see Fig. 8(e)]. Using other resolution images and scale parameters to detect small and simple craters inside groups is better [see Fig. 8(f)]. Three crater communities are clearly separated in the 120-m/pixel image using the 360 scale parameter [see Fig. 8(h)]. Crater communities are large-scale spatial features compared with small craters, so coarse pixel size images also work well when they demonstrate clear boundaries. One ghost community is missed in the right corner of the image [see Fig. 8(i)] because the rim of the old ghost crater had been heavily modified. For the ghost crater community, the scale parameter needed to be adjusted to first find the inner part inside the community and then infer the whole rim of the community.

Changing the scale parameter during image segmentation will change the spatial delineation of an object, its shape, and the spatial relationship between different object types and backgrounds [68]. Pixel-based classifications of panchromatic images with 1-m spatial resolution may be sufficient to detect small craters at fine scales. However, aggregation of pixels into objects is required to identify other bigger crater types at coarse scales. The scale parameters control the accuracy of the aggregation of pixels into objects. Pixels are spatially autocorrelated under the scaling threshold in the scope of feature lag distance of semivariogram models corresponding to certain spatial resolutions. Multiscale parameters should be used to extract different crater types from corresponding resolution images. As the resolution decreases, smaller-scale parameters should be used to extract crater types located at lower levels of the spatial structure to avoid under-segmentation. Conversely, larger-scale parameters should be used to extract crater types located at higher levels of the spatial structure to avoid over-segmentation. Identifying the scaling threshold the semivariogram analysis can balance over-segmentation and under-segmentation when adjusting the size of image objects through the scale parameter [69].

#### IV. CONCLUSION

This article focused on studying the coupling relationship among the spatial structures of craters, resolution of remote sensing optical images and scale parameters. Spatial variance is the meta-expression of spatial patterns and morphological characteristics in a remote sensing perspective. Next, with the fast development of lunar exploration programs, massive multiresolution imageries are available for investigating the spatial patterns and morphological characteristics of lunar crater, which inevitably leads to the challenge of detecting the spatial variation of an object using various spatial resolutions and scale parameters. Because semivariogram model can provide rich spatial information at different lag distances, we employed its indicators as quantitative measures to characterize the multiscale hierarchical spatial structures of lunar craters. A semivariogram analysis of the spatial structures of craters revealed that defining a spatial resolution is problematic, especially when the structure contains multiple scales of craters rather than a specific one. Semivariogram models indicated that the optimum spatial

resolutions for different levels of craters contained in the spatial structure are 1, 7, 20, 50, and 120 m. Medium spatial resolutions could be used to detect two or three levels of craters at the same time. The feature lag distances of the semivariogram model indicate that a series of appropriate spatial resolutions rather than a single spatial resolution is required to address multiscale lunar impact crater structures. Also semivariogram models indicated that scale parameters for different levels of craters contained in the spatial structure vary with spatial resolutions. The detection accuracy is between 72.7% and 90.9% of the different crater types in the spatial structure in the selected regions, in which small craters are well-distinguished compared with other CDAs. The average values of  $R_{in}$  and  $R_{out}$  when evaluating the results from the perspective of the geometry of the detected craters are 85.2% and 8.4%, respectively, which indicate that the coupling relationship among the spatial structures of craters, resolution of remote sensing optical images and scale parameters presented by the algorithm is applicable. The selection of optimum spatial resolutions and scale parameters is image and site dependent. Different range values from the semivariogram models might be applied to different images to map similar spatial crater structures due to the variation of object spectral reflectance responses between images. The main contribution of this article is the use of a classic geostatistical method to quantify the relationship between spatial structures of lunar craters, spatial resolutions, and scale parameters. This quantified relationship is essential to addressing multiscale crater mapping and the application of information on spatial structures for crater evolution. However, the results of this article were limited to the selected images, geostatistical method, and study site. In future studies, we may present our method integrating machine learning techniques on the basis of different data sources to clarify the relationship among the extraction of geomorphological features on extraterrestrial bodies, image quality, and segment thresholds.

#### ACKNOWLEDGMENT

The authors would like to thank all the organizations for sharing their data. They would also like to thank the editor and the anonymous reviewers for their detailed suggestions and constructive comments.

#### REFERENCES

- [1] G. McGill, "Morphology of lunar craters: A test of lunar erosional models," *Icarus*, vol. 21, no. 4, pp. 437–447, 1974.
- [2] T. V. Gasiganti *et al.*, "An object-based classification method for automatic detection of lunar impact craters from topographic data," *Adv. Space Res.*, vol. 57, pp. 1978–1988, 2016.
- [3] J. P. Cohen, "Automated crater detection using machine learning," Ph.D. dissertation, Dept. Electron. Eng., Univ., City of Univ. of Massachusetts, Boston, MA, USA, 2016.
- [4] P. Senthil Kumar *et al.*, "Gullies and landslides on the moon: Evidence for dry-granular flows," *J. Geophys. Res.-Planet*, vol. 118, no. 2, pp. 206–223, 2013.
- [5] P. Kumar, J. Head, and D. Kring, "Erosional modification and gully formation at meteor crater, Arizona: Insights into crater degradation processes on mars," *Icarus*, vol. 208, no. 2, pp. 608–620, 2010.
- [6] J. Wang *et al.*, "Automatic mapping of lunar landforms using DEM-derived geomorphometric parameters," *J. Geography. Sci.*, vol. 27, no. 11, pp. 1413–1427, 2017.
- [7] M. Chandnani, R. Herrick, and G. Kramer, "Geologic analyses of the causes of morphological variations in lunar craters within the simple-to-complex transition," *J. Geophys. Res.-Planet*, vol. 124, pp. 1238–1265, 2019.
- [8] M. Kamal, S. Phinn, and K. Johansen, "Object-based approach for multi-scale mangrove composition mapping using multi-resolution image datasets," *Remote Sens.*, vol. 7, no. 4, pp. 4753–4783, 2015.
- [9] G. Louw and A. van Niekerk, "Object-based land surface segmentation scale optimisation: An ill-structured problem," *Geomorphology*, vol. 327, pp. 377–384, 2019.
- [10] C. Giri *et al.*, "Status and distribution of mangrove forests of the world using earth observation satellite data," *Global Ecol. Biogeog.*, vol. 20, no. 1, pp. 154–159, 2010.
- [11] S. Toure *et al.*, "Land cover and land use change analysis using multi-spatial resolution data and object-based image analysis," *Remote Sens. Environ.*, vol. 210, pp. 259–268, 2018.
- [12] J. Wang *et al.*, "Quantifying and characterizing the dynamics of urban greenspace at the patch level: A new approach using object-based image analysis," *Remote Sens. Environ.*, vol. 204, pp. 94–108, 2018.
- [13] S. Rajbhandari *et al.*, "Leveraging machine learning to extend ontology-driven geographic object-based image analysis (O-GEOBIA): A case study in forest-type mapping," *Remote Sens.*, vol. 11, no. 5, pp. 503–528, 2019.
- [14] D. Davis, "Object-based image analysis: A review of developments and future directions of automated feature detection in landscape archaeology," *Archaeol. Prospection*, vol. 26, no. 2, pp. 155–163, 2018.
- [15] R. Comert *et al.*, "Mapping of shallow landslides with object-based image analysis from unmanned aerial vehicle data," *Eng. Geol.*, vol. 260, 2019, Art. no. 105264.
- [16] H. Zhao *et al.*, "Extraction of terraces on the Loess plateau from high-resolution DEMs and imagery utilizing object-based image analysis," *ISPRS Int. J. Geo-Inf.*, vol. 6, no. 6, pp. 157, 2017.
- [17] M. Hossain and D. Chen, "Segmentation for object-based image analysis (OBIA): A review of algorithms and challenges from remote sensing perspective," *ISPRS J. Photogrammetry*, vol. 150, pp. 115–134, 2019.
- [18] D. Jelinski and J. Wu, "The modifiable areal unit problem and implications for landscape ecology," *Landscape Ecol.*, vol. 11, no. 3, pp. 129–140, 1996.
- [19] Y. He, X. Guo, and B. C. Si, "Detecting grassland spatial variation by a wavelet approach," *Int. J. Remote Sens.*, vol. 28, no. 7, pp. 1527–1545, 2007.
- [20] S. Zhang *et al.*, "The scale effect on spatial interaction patterns: An empirical study using taxi O-D data of Beijing and Shanghai," *IEEE Access*, vol. 6, pp. 51994–52003, 2018.
- [21] T. Pei *et al.*, "A new insight into land use classification based on aggregated mobile phone data," *Int. J. Geography Inf. Sci.*, vol. 28, no. 9, pp. 1988–2007, 2014.
- [22] Y. Liu *et al.*, "Social sensing: A new approach to understanding our socioeconomic environments," *Ann. Assoc. Amer. Geography*, vol. 105, no. 3, pp. 512–530, 2015.
- [23] X. Liu *et al.*, "Incorporating spatial interaction patterns in classifying and understanding urban land use," *Int. J. Geography Inf. Sci.*, vol. 30, no. 2, pp. 334–350, 2015.
- [24] M. Kamal, S. Phinn, and K. Johansen, "Object-based approach for multi-scale mangrove composition mapping using multi-resolution image datasets," *Remote Sens.*, vol. 7, no. 4, pp. 4753–4783, 2015.
- [25] R. Platt and L. Rapoza, "An evaluation of an object-oriented paradigm for land use/land cover classification," *Professional Geography*, vol. 60, no. 1, pp. 87–100, 2008.
- [26] M. Möller, L. Lyburner, and M. Volk, "The comparison index: A tool for assessing the accuracy of image segmentation," *Int. J. Appl. Earth Obs.*, vol. 9, no. 3, pp. 311–321, 2007.
- [27] T. Kavzoglu, M. Yildiz Erdemir, and H. Tonbul, "A region-based multi-scale approach for object-based image analysis," *ISPRS Int. Arch. Photogrammetry*, vol. 7, pp. 241–247, 2016.
- [28] L. Drăguș, C. Eisank, and T. Strasser, "Local variance for multi-scale analysis in geomorphometry," *Geomorphology*, vol. 130, no. 3–4, pp. 162–172, 2011.
- [29] V. Srivastava *et al.*, "Simulated annealing with variogram-based optimization to quantify spatial patterns of trees extracted from high-resolution images," *IEEE Geosci. Remote Sens. Lett.*, vol. 13, no. 8, pp. 1084–1088, Aug. 2016.
- [30] D. Ming *et al.*, "Semivariogram-based spatial bandwidth selection for remote sensing image segmentation with mean-shift algorithm," *IEEE Trans. Geosci. Remote Sens. Lett.* vol. 9, no. 5, pp. 813–817, Sep. 2012.
- [31] W. Ma *et al.*, "Achieving super-resolution remote sensing images via the wavelet transform combined with the recursive Res-Net," *IEEE Trans. Geosci. Remote Sens.*, vol. 57, no. 6, pp. 3512–3527, Jun. 2019.

- [32] H. Chen *et al.*, "Spatial upscaling of remotely sensed leaf area index based on discrete wavelet transform," *Int. J. Remote Sens.*, vol. 40, no. 5/6, pp. 2343–2358, 2019.
- [33] P. Curran, "The semivariogram in remote sensing: An introduction," *Remote Sens. Environ.*, vol. 24, no. 3, pp. 493–507, 1988.
- [34] M. Kamal, S. Phinn, and K. Johansen, "Assessment of mangrove spatial structure using high-spatial resolution image data," *Int. Geosci. Remote Sens.*, vol. 92, no. 10, pp. 2609–2612, 2013.
- [35] S. Colombo, "Variographic analysis of tropical forest cover from multi-scale remotely sensed imagery," *ISPRS J. Photogrammetry*, vol. 58, no. 5–6, pp. 330–341, 2004.
- [36] P. Treitz, "High spatial resolution remote sensing data for forest ecosystem classification: an examination of spatial scale," *Remote Sens. Environ.*, vol. 72, no. 3, pp. 268–289, 2000.
- [37] J. Weishampel *et al.*, "Semivariograms from a forest transect gap model compared with remotely sensed data," *J. Vegetation Sci.*, vol. 3, no. 4, pp. 521–526, 1992.
- [38] M. A. Oliver *et al.*, "Semi-variograms for modelling the spatial pattern of landform and soil properties," *Earth Surf. Processes Landforms*, vol. 11, pp. 491–504, 1986.
- [39] D. Ryu and J. Famiglietti, "Multi-scale spatial correlation and scaling behavior of surface soil moisture," *Geophys. Res. Lett.*, vol. 33, no. L08404, pp. 1–4, 2006.
- [40] A. Oldak, T. Jackson, and Y. Pachepsky, "Using GIS in passive microwave soil moisture mapping and geostatistical analysis," *Int. J. Geography Inf. Sci.*, vol. 16, no. 7, pp. 681–698, 2002.
- [41] C. Murillo Feo, L. Martinez Martinez, and N. Correa Muñoz, "Accuracy and spatial variability in GPS surveying for landscape mapping on road inventories at a semi-detailed scale: The case in Colombia," *ISPRS Int. Arch. Photogrammetry*, vol. 2, pp. 291–297, 2016.
- [42] C. Robb *et al.*, "A semi-automated method for mapping glacial geomorphology tested at Breiðamerkurjökull, Iceland," *Remote Sens. Environ.*, vol. 163, pp. 80–90, 2015.
- [43] J. Karl and B. Maurer, "Multivariate correlations between imagery and field measurements across scales: Comparing pixel aggregation and image segmentation," *Landscape Ecol.*, vol. 25, no. 4, pp. 591–605, 2009.
- [44] P. Atkinson and P. Aplin, "Spatial variation in land cover and choice of spatial resolution for remote sensing," *Int. J. Remote Sens.*, vol. 25, no. 18, pp. 3687–3702, 2004.
- [45] A. Rahman *et al.*, "Optimum pixel size for hyperspectral studies of ecosystem function in Southern California chaparral and grassland," *Remote Sens. Environ.*, vol. 84, no. 2, pp. 192–207, 2003.
- [46] B. Zhao *et al.*, "Overall scheme and on-orbit images of chang'E-2 lunar satellite CCD stereo camera," *Sci. China Tech. Sci.*, vol. 54, no. 9, pp. 2237–2242, 2011.
- [47] R. Vondrak, J. Keller, G. Chin, and J. Garvin, "Lunar reconnaissance orbiter (LRO): Observations for lunar exploration and science," *Space Sci. Rev.*, vol. 150, no. 1–4, pp. 7–22, 2010.
- [48] S. Jin, S. Arivazhagan, and H. Araki, "New results and questions of lunar exploration from SELENE, chang'E-1, Chandrayaan-1 and LRO/LCROSS," *Adv. Space Res.*, vol. 52, no. 2, pp. 285–305, 2013.
- [49] M. S. Robinson *et al.*, "Lunar reconnaissance orbiter camera (LROC) instrument overview," *Space Sci. Rev.*, vol. 150, no. 1–4, pp. 81–124, 2010.
- [50] "Lunar map (LM) series," Defense Mapping Agency, Fort Belvoir, VA, USA, 1979. [Online]. Available: <https://www.lpi.usra.edu/resources/mapcatalog/LM/>
- [51] Z. Lin *et al.*, "Spatial analysis of carbon storage density of mid-subtropical forests using geostatistics: A case study in Jiangle county, Southeast China," *Acta Geochimica*, vol. 37, no. 1, pp. 90–101, 2017.
- [52] G. Matheron, "Principles of geostatistics," *Econ. Geol.*, vol. 58, no. 8, pp. 1246–1266, 1963.
- [53] P. Curran, "The semivariogram in remote sensing: An introduction," *Remote Sens. Environ.*, vol. 24, no. 3, pp. 493–507, 1988.
- [54] F. Miranda, L. Fonseca, and J. Carr, "Semivariogram textural classification of JERS-1 (Fuyo-1) SAR data obtained over a flooded area of the amazon rainforest," *Int. J. Remote Sens.*, vol. 19, no. 3, pp. 549–556, 1998.
- [55] P. Atkinson and P. Curran, "Defining an optimal size of support for remote sensing investigations," *IEEE Trans. Geosci. Remote*, vol. 33, no. 3, pp. 768–776, May 1995.
- [56] A. B. McBratney and W. Webster, "Spatial dependence and classification of the soil along a transect in north-east Scotland," *Geoderma*, vol. 26, pp. 63–82, 1981.
- [57] R. Webster and S. Nortcliff, "Improved estimation of micro nutrients in hectare plots of the sonning series," *J. Soil Sci.*, vol. 35, no. 4, pp. 667–672, 1984.
- [58] J. McGrew and C. Monroe, *An Introduction to Statistical Problem Solving in Geography*, 2nd ed. Boston, MA, USA: McGraw-Hill, 2000, pp. 110.
- [59] *Trimble Germany GmbH, Ecognition Developer 8.7.2 Reference Book*. Munich, Germany: Trimble Germany GmbH, 2011.
- [60] M. Chen *et al.*, "Lunar crater detection based on terrain analysis and mathematical morphology methods using digital elevation models," *IEEE Trans. Geosci. Remote Sens.*, vol. 56, no. 7, pp. 3681–3692, Jul. 2018.
- [61] D. Liu *et al.*, "Boundary detection of dispersal impact craters based on morphological characteristics using lunar digital elevation model," *IEEE J. Sel. Topics Appl. Earth Observ. Remote Sens.*, vol. 10, no. 12, pp. 5632–5646, Dec. 2017.
- [62] T. Zhang, S. Jin, and H. Cui, "Automatic detection of martian impact craters based on digital elevation model," *J. Deep Space Exploration*, vol. 1, pp. 123–127, 2014.
- [63] J. Wang, W. Cheng, and C. Zhou, "A chang'e-1 global catalog of lunar impact craters," *Planet Space Sci.*, vol. 112, pp. 42–45, 2015.
- [64] J. Cohen, Automated crater detection using machine learning. Ph.D. dissertation, Dept. Elect. Eng., Univ. Massachusetts, Boston, MA, USA, Jun. 2016.
- [65] L. Bandeira, W. Ding, and T. F. Stepinski, "Automatic detection of Sub-km craters using shape and texture information," in *Proc. 41st Lunar Planet. Sci. Conf.*, Mar. 2010.
- [66] C. Szegedy *et al.*, "Going deeper with convolutions," in *Proc. IEEE Conf. Comput. Vis. Pattern Recognit.*, 2015, pp. 1–9.
- [67] C. Lee, "Automated crater detection on mars using deep learning," *Planet Space Sci.*, vol. 170, pp. 16–28, 2019.
- [68] S. Lowe and X. Guo, "Detecting an optimal scale parameter in object-oriented classification," *IEEE J. Sel. Topics Appl.*, vol. 4, no. 4, pp. 890–895, Dec. 2011.
- [69] J. Karl and B. Maurer, "Multivariate correlations between imagery and field measurements across scales: Comparing pixel aggregation and image segmentation," *Landscape Ecol.*, vol. 25, no. 4, pp. 591–605, 2009.



**Jiao Wang** received the Ph.D. degree from the Institute of Geographic Sciences and Natural Resources Research, Chinese Academy of Sciences, Beijing, China.

She is currently an Associate Professor with the School of Information Engineering, the China University of Geosciences, Beijing, China, and a Visiting Scholar with the State Key Laboratory of Resources and Environmental Information System, Institute of Geographic Sciences and Natural Resources Research, Chinese Academy of Sciences, Beijing, China. These studies have included topographical and spectral understanding of planetary landform, spatial and temporal heterogeneity characterization of planetary landform, classification, as well as change detection of planetary landform.



**Dongping Ming** received the Ph.D. degree from the Institute of Geographic Sciences and Natural Resources Research, Chinese Academy of Sciences, Beijing, China.

She is currently a Professor with the School of Information Engineering, China University of Geosciences, Beijing, China. Her research interests include intelligent processing and analysis of remote sensing imagery, information extraction from high resolution remote sensing imagery, related issues about spatio-temporal scale, and GIS application.



**Weiming Cheng** received the Ph.D. degree from the Institute of Geographic Sciences and Natural Resources Research, Chinese Academy of Sciences, Beijing, China. He is a Professor with the State Key Laboratory of Resources and Environmental Information System, Institute of Geographic Sciences and Natural Resources Research, Chinese Academy of Sciences, Beijing, China.

His research include digital terrain analysis with studies covering quantitative extraction and mapping of digital landform information; land suitability evaluation; rapid disaster assessment; analysis of ecological and environmental changes based on topography and landform.